Interfacial magnetic characteristics of nearly compensated gadolinium iron garnet

Karthik Srinivasan,[1,7,*] Alexander J. Grutter,[2] Thomas E. Gage,[3] P. Quarterman,[2] Christy J. Kinane,[4] Andrew J. Caruana,[4] Guichuan Yu,[5,6] Javier Garcia-Barriocanal,[5] Sean Langridge,[4] and Bethanie J. H. Stadler[1,†]

[1]*Department of Electrical and Computer Engineering, University of Minnesota, 200 Union Street SE, Minneapolis, Minnesota 55455, USA* [2]*NIST Center for Neutron Research, National Institute of Standards and Technology, Gaithersburg, Maryland 20878, USA*

[3]*Center for Nanoscale Materials, Argonne National Laboratory, Lemont, Illinois 60439, USA*

[4]*ISIS-Neutron and Muon Source, STFC Rutherford Appleton Laboratory, Didcot, Oxfordshire, OX11 0QX, United Kingdom*

[5]*Characterization Facility, University of Minnesota, 100 Union Street SE, Minneapolis, Minnesota 55455, USA*

[6]*Institute of Informatics, University of Minnesota, 2231 6th Street SE, Minneapolis, Minnesota 55455, USA*

[7]*Department of Electrical and Computer Engineering, Boise State University, Boise, Idaho 83725, USA*

Reports on spin Hall magnetoresistance, magnonic spin currents from thermal gradients, and spin transfertorque magnetic random-access memory using compensated ferrimagnets largely discuss bulk magnetization but lack consideration of depth profiles or interfacial characteristics. Here, magnetic and structural characterization of profiles and interfaces was performed for nearly compensated gadolinium iron garnet (GdIG) thin films. X-ray diffraction and reciprocal space maps show that sputter deposited GdIG on Si is polycrystalline with the desired cubic garnet phase, and GdIG on gadolinium gallium garnet (GGG) is epitaxial with <0.06% compressive strain. Temperature-dependent magnetometry confirms the compensation temperatures of GGG/GdIG and Si/GdIG to be 285 and 260 K, respectively, both near room temperature. Interestingly, these measurements suggest the presence of unsaturated rare-earth moments, which result in a characteristic hysteresis between heating and cooling sequences in the magnetization-temperature curves at zero field. Depth-profile measurements from polarized neutron reflectometry (PNR) indicate up to 91% volume fraction in GdIG on Si. At the interface, PNR reveals a region containing magnetized Fe-doped GGG, a low-density GdIG at the GGG/GdIG interface, and a thin magnetically dead layer at the Si/GdIG interface. Cross-sectional transmission electron microscopy and energy dispersive x-ray spectroscopy confirm the assessment of PNR. The magnetic characteristics of interfacial regions are attributed to intermixing of Fe-Ga at the GGG/GdIG interface and the presence of amorphous Fe-Si at the Si/GdIG interface.

the film remains a critical challenge on the road to compensated ferrimagnet spintronics.

No materials class exemplifies this challenge more than the rare-earth iron garnets, which are promising for their enormous range of tunable magnetic anisotropies and compensation temperatures [9–15]. Despite their desirable properties, high-quality iron garnet thin films have been largely restricted to growth on garnet substrates such as gadolinium gallium garnet (GGG or $Gd_3Ga_5O_{12}$) and plagued by reports of cation intermixing at the interface [16–18]. While some work has focused on understanding the intermixing problem in compensated garnets, most is focused on $Y_3Fe_5O_{12}$ (YIG), which does not have a magnetic compensation point [13,16,17,19]. Thus more work is critically needed to understand interfacial effects on technologically relevant rare-earth iron garnets. Therefore we have probed and isolated the bulk and interfacial magnetic properties of gadolinium iron garnet (GdIG), which has attracted recent attention for its near-room-temperature compensation point and the strong temperature-dependent magnetization of the gadolinium sublattice. GdIG is particularly interesting from the perspective of intermixing studies because it has the same rare-earth cation as GGG substrates so that the only relevant intermixing issue is that of

Fe-Ga exchange. In order to understand the behavior of GdIG magnetic interfaces, the role of cation interdiffusion, and the suitability of GdIG for incorporation into Si-based device heterostructures, we compare samples grown on both GGG substrates and Si/SiO_2.

Previous research has typically used GdIG to study spin transport efficiency, and its correlation with the different magnon modes and sublattice magnetizations using longitudinal spin Seebeck effect (SSE) measurements [20–22]. For instance, Geprägs *et al*. attribute the polarity inversion of the SSE current at two distinct temperatures to a uniform precession mode and an optical mode in the spin-wave spectra, but do not consider interfacial effects due to a lack of experimental evidence [23]. Additionally, theoretical considerations of these magnon modes and their coupling with phonons from lattice vibrations usually assume uniform magnetic properties (and a homogeneous magnetic compensation) across the thickness of the garnet film [24,25]. Even systematic reports on the magnetic and structural properties of single and polycrystalline GdIG are restricted to the discussion of bulklike magnetization and lack a thorough consideration of homogeneity across the depth profile or interfacial characteristics [26–28]. Only recently has the presence of two strain levels at the interface and in the rest of the film, respectively, been reported for GdIG films grown on substituted gadolinium gallium garnet (SGGG) substrates [29]. Reports are emerging that use compensated ferrimagnets for spin Hall magnetoresistance (SMR) [4,30], magnonic spin currents from a thermal gradient (SSE) [25,31], and the possibility of a spin transfertorque magnetic random-access memory (STT MRAM) [32]. These reports necessitate a thorough characterization of the interface and homogeneity of structural and magnetic properties in GdIG thin films.

This paper investigates the structural, compositional, and magnetic characteristics of single crystalline and polycrystalline GdIG thin films on GGG and Si substrates using a variety of bulk- and depth-dependent techniques. While the bulk properties are obtained using x-ray diffraction, energy dispersive spectroscopy (EDS), and magnetometry, the investigation of elemental and magnetic profiles, along with buried interfacial magnetism are carried out using polarized neutron reflectometry (PNR), cross-section scanning transmission electron microscopy (STEM), and high-resolution transmission electron microscopy (HRTEM). Complex techniques like PNR allow for simultaneous measurement of the chemical composition and in-plane magnetization as a function of depth in thin film systems, while avoiding paramagnetic substrate (GGG) noise that is typical in bulk magnetometry. In particular, PNR has proven to be insightful in elucidating complex magnetic interactions in garnets, including those caused by interdiffusion and heterostructure formation with nongarnet systems [17,33]. On the other hand, HRTEM and STEM measurements complement the findings of PNR, and provide an accurate elemental and structural quantification at the GdIGsubstrate interfaces.

II. METHODS

A. Thin film deposition

Thin films of GdIG were sputter deposited on silicon and GGG (100) substrates from elemental targets of Gd and Fe in a reactive radio frequency magnetron sputtering system with a 10:1 ratio of Ar:O_2. The sputtering system had a top-down sputter configuration, where the substrates sat on a rotating stage at a distance of 10 cm from the sputtering sources. The

deposition process was carried out at room temperature, and the as-deposited amorphous films on Si/SiO_2 and GGG were annealed at 900° C for 3 min in a 10 SCCM (cubic centimeters per minute at STP) (7.5 μmol/s) flow of O_2. The ramp-up rate was >200 C/s and the ramp-down rate was ~40 C/s.

B. Structural and elemental characterization

The thickness of the films was measured using a KLA Tencor P-16 surface profilometer. Structural x-ray patterns were measured on a Bruker D8 Discover microdiffractometer equipped with a Co ($K\alpha$) source of wavelength 1.79Å, which was conditioned with a graphite monochromator, a quartercircle Eulerian cradle, and a Våntec-500 two-dimensional detector that covered approximately a 30° range of both two theta and chi angles. A cobalt x-ray source was chosen to reduce the fluorescence of the Fe from the sample. Polycrystalline peaks were identified with a database reference (PDF #01-072-0141) corresponding to cubic gadolinium iron garnet ($Gd_3Fe_5O_{12}$, space group: *Ia*-3*d*) using MDI JADE. Comparisons with the reference pattern for $GdFeO_3$ (PDF #01-074-1476) do not indicate the presence of a secondary phase. Three-dimensional reciprocal space maps were constructed using the RSLAB program [33] developed by the Characterization Facility at the University of Minnesota. Elemental composition was determined using an Oxford electron dispersive spectroscopy (EDX) detector in a JEOL 6500F scanning electron microscope (SEM). The beam was set to 15 kV with maximum probe current available. Quantitative data processing was carried out in AZTEC nanoanalysis software by Oxford Instruments. Owing to the presence of Gd in both GGG substrate and GdIG films, an accurate estimation of Gd stoichiometry through SEM EDS was not possible.

C. Magnetometry

Magnetic hysteresis measurements were recorded using a Quantum Design MPMS3 in the vibrating sample magnetometer (VSM) mode between 10 and −10 kOe. Temperature-dependent *M*-*H* and *M* vs *T* measurements were carried out using a helium-based cryogenic susceptometer. In measurements where the temperature was swept while recording magnetization, the sample was saturated and centered first, and then the temperature was swept in either a zero field or a saturation field of 2000 Oe between 20 and 400 K.

D. Polarized neutron reflectometry

Polarized neutron reflectometry measurements were performed on GdIG films grown on Si and GGG substrates using the POLREF instrument at the ISIS Neutron and Muon Source [34]. The POLREF beamline is a white beam time of flight (TOF) polarized neutron reflectometer with a polarized wavelength band of 2 − 14Å. The sample was mounted flat, with gravity normal to the surface, in a helium flow cryostat, itself mounted in a GMW magnet with a maximum field of ±0.7 T that can be applied in the plane of the sample. A helium exchange gas pressure of 4 kPa was used, providing a temperature stability of ±0.01 K. The sample was held in place by gravity alone; no epoxy was used to avoid bending issues at low temperatures.

Data modeling was performed using the REFL1D software package. This system represents a particular challenge due to the wavelength-dependent complex scattering factors associated with Gd (see Ref. [35]). The wavelength variation is relatively slow at wavelengths above 3Å, and typical PNR measurements utilizing the wavelength range of POLREF are analyzed by treating the entire dataset with a single wavelength-averaged Gd scattering cross section. However, this approach may not be appropriate when extracting precise Gd stoichiometries, as we do here. To address this, we have separated each measured angle into four wavelength bins of 2.0 − 2.5Å, 2.5 − 3.0Å, 3.0 − 4.5Å, and 4.5 − 12Å, and performed the analysis on the unstitched data. As most of the wavelength variation occurs below 3Å, and the scattering factors are essentially constant above 4.5Å, further subdivision is unnecessary [35]. We consider both the real and imaginary scattering length density (SLD) contributions of the Gd wavelength dependence. The imaginary SLD, representing neutron absorption, arises almost exclusively from the Gd in these samples, and is therefore the best and most reliable representative of Gd content. We calculate the mean theoretical imaginary SLDs for ideal GdIG to be 1.59×10^{-4}, 1.50×10^{-4}, and 1.40×10^{-4} nm^{-2} for the 2.0 − 2.5Å, 2.5 − 3.0Å, 3.0 − 4.5Å, and 4.5 − 12Å wavelength bins, respectively. The same calculation was performed for the GGG layers. While these values will vary with the Gd stoichiometry, the ratio between the imaginary SLDs must be preserved. We therefore fit the imaginary SLDs of all the wavelength bins using a single parameter in the model and constrained all the wavelength bins to maintain the expected theoretical ratio in the imaginary SLDs. A similar calculation was performed for the real component of the nuclear SLD, but the effect is a much smaller fraction of the overall scattering factor due to contributions from other nuclei. Nevertheless, the wavelengthdependent constraint was rigorously enforced for the real component, even though the imaginary SLD is considered to be a much better measure of the total Gd content within a given layer. We note that comparison of fits performed using two wavelength bands instead of four returned essentially the same χ^2 goodness of fit and parameter values, while a single wavelength band was clearly insufficient. We therefore conclude that the use of four wavelength bands is more than sufficient to properly describe the data. PNR measurements were also taken at two different magnetic fields, which were corefined to models with different magnetic SLD profiles but the same nuclear SLD profile. The data presented in the results were stitched and rebinned into a single curve following the fitting analysis, for a clear presentation.

E. Transmission electron microscopy

TEM experiments were carried out using a Thermo Fisher Talos, at the Center for Nanoscale Materials, ANL. TEM samples were prepared by typical cross-section methods using a Zeiss Nvision but intentionally left >200 nm thick. Finally, polishing was performed with Ar in a Gatan PIPS II to avoid Ga from the FIB which may have influenced the STEM EDS analysis. Samples were then investigated by HRTEM, STEM, and EDS at an accelerating voltage of 200kV. The Talos is equipped with an extreme field emission gun (XFEG) for extra-high brightness and four silicon drift detectors for a large solid collection angle to improve the signal-to-noise ratio of EDS mapping.

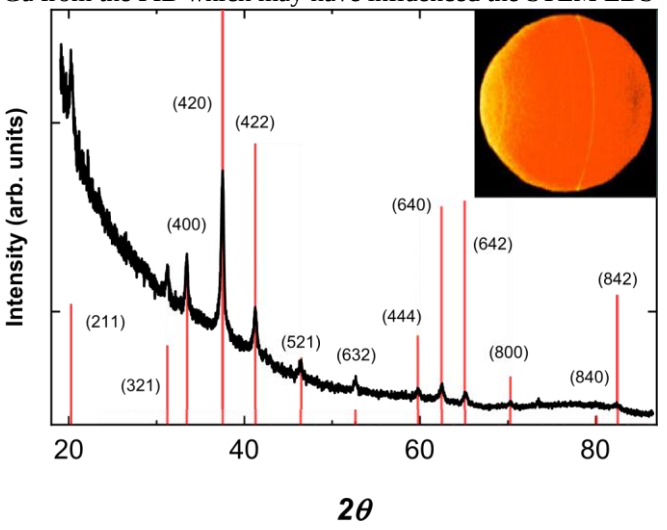

FIG. 1. X-ray powder diffraction of the Si/GdIG (72 nm) sample. The peaks corresponding to different orientations indicate the untextured polycrystalline nature of the films. The inset shows the first detector image measured to obtain the scan center at 32° with fixed omega of 16°.

III. RESULTS AND DISCUSSION

Composition analysis of the GdIG on Si using energy dispersive x-ray spectroscopy (EDS) in a scanning electron microscope (SEM) approximates 18% − 20% Gd deficiency relative to the stoichiometric value of 15% Gd in $Gd_3Fe_5O_{12}$. Similar analysis on GGG/GdIG using STEM EDS reveals excellent agreement between the samples, with Gd deficiency on the order of 20% − 22%. It is likely that the deficiencies in sputter yields of the Fe and Gd targets are from oxidation in a reactive process, resulting in lower cation ratios in the sputtered thin film [36]. These deviations from stoichiometry could result in different cation oxidation states as reported elsewhere [37,38]. The x-ray diffraction pattern in Fig. 1 shows that a 72 nm GdIG film on Si is polycrystalline with isotropically oriented grains producing the diffraction cones shown in the inset of Fig. 1. The thin film is in the desired cubic garnet crystal phase, as observed from comparing the data to the database reference (PDF #01-072-0141) represented with the red vertical lines in Fig. 1. The cubic garnet has an average lattice constant of 12.425Å calculated from the (400), (420), and (422) diffraction peak positions. The powder XRD scan was measured at three detector positions, with centers of 32°, 52°, and 72°, which results in a 2θ observation range of 70°. During the data collection for each detector position, the incident angle (θ) was fixed at 16°, 26°, and 36°, respectively. This measurement configuration avoids the contribution of the substrate (0 0 *L*) diffraction peaks to the diffractogram, since the geometrical Bragg conditions are not accomplished,

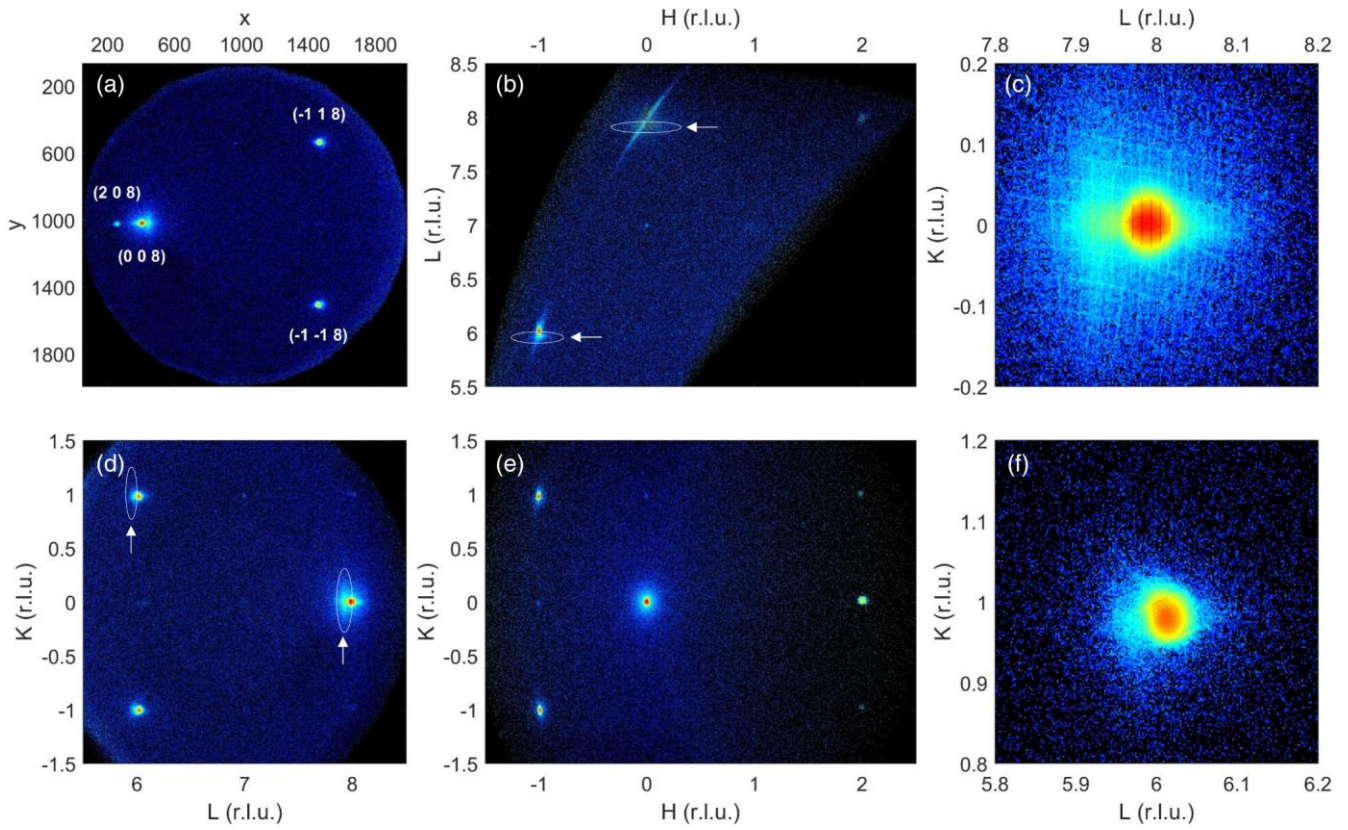

FIG. 2. Three-dimensional reciprocal space map of the GGG/GdIG (66 nm) sample. (a) X-ray detector image in detector pixel coordinates. (b) *HL* projection. (c) Magnified *KL* projection of the (008) peak. (d) *KL* projection. (e) *HK* projection. (f) Magnified *KL* projection of the asymmetric (1–18) peak.

highlighting only the powder rings from the isotropic crystalline structure of the film.

On the other hand, 66 nm of GdIG films deposited on lattice-matched GGG substrates are highly crystalline with a texture along the (0 0 *L*) crystallographic direction similar to the one expected for epitaxial films. The x-ray scattering study on this sample shows an absence of powder diffraction rings and allows us to obtain a three-dimensional reciprocal space map (RSM) using the technique described in Ref. [39]. The maps are constructed using 191 images that were measured with a 2θ detector position of 60° as a function of omega, which ranges from 20.5° to 39.5° at increments of 0.1° as shown in Figs. S1–S3 in the Supplemental Material [40]. We convert each pixel of the 191 images into the reciprocal space units of the substrate, which serves as crystallographic reference. The results are shown in Fig. 2, where Fig. 2(a) shows the stack of the x-ray detector images in the detector pixel coordinates. The four high-intensity single crystal peaks of the substrate that are observed here were used to obtain its orientation matrix. The converted *HL*, *KL*, and *HK* projections of the data are shown in Figs. 2(b), 2(d), and 2(e), respectively. They reveal three asymmetric substrate reflections (2 0 8), (–1 1 8), and (−1 − 18), and the corresponding (0 0 8) symmetric reflection. A careful look at the structure of the diffraction peaks reveals the presence of peaks with much lower intensity at smaller *L* values with respect to those observed for the (0 0 8), (−118), and (−1 −1 8) peaks of the substrate. These lower-intensity peaks are highlighted with white arrows and ellipses and they correspond to the GdIG thin film. This is better observed in the magnified RSM of the *KL* projection of the (0 0 8) and (1 −1 8) peaks in Figs. 2(c) and 2(f). The data are consistent with a highly textured, epitaxial-like thin film that matches the real space *ab* plane of the substrate, which produces an in-plane compressive strain <0.06% and an out-of-plane traction of the film.

Cations in a unit cell of GdIG are distributed between three magnetic sublattices, where the rare-earth sublattice (Gd^{3+}) from dodecahedral sites is coupled antiferromagnetically to the net Fe^{3+} sublattice moment from tetrahedral and octahedral sites. Since the Gd^{3+} moments are large and have a strong temperature dependence, their associated magnetization contribution is sharply reduced at higher temperatures. The magnetization of GdIG is consequently dominated by Fe^{3+} sublattices near room temperature and the Gd^{3+} sublattice at lower temperatures. This is reflected in the magnetic hysteresis loops shown in Figs. S4 and S5 in the Supplemental Material [40], where the in-plane saturation magnetization for GdIG/GGG [Fig. S4(a)] and GdIG/Si [Fig. S5(a)] decrease at higher temperatures and approach zero near the magnetic compensation points. Correspondingly, as the temperature increases, the Gd^{3+} moment decreases and becomes increasingly unsaturated due to thermal fluctuations, which in the presence of a Fe^{3+} sublattice with large spontaneous magnetization gives rise to an exchange-enhanced

paramagnetic susceptibility [41,42]. Therefore, at compensation, the reduced Gd^{3+} moment and a large differential susceptibility ($\chi_d = dM/dH$) from the paramagnetic contribution render the garnet to effectively a single domain of Fe^{3+} resulting in a divergence of the coercive field as shown in Figs. S4(b) and S5(b) [40]. It must be noted that the single domain theory only captures the phenomenology of diverging coercivity, but in practice, reversal through domain walls, coarse domain structures, and unsaturated Gd^{3+} limit the coercivity to finite values.

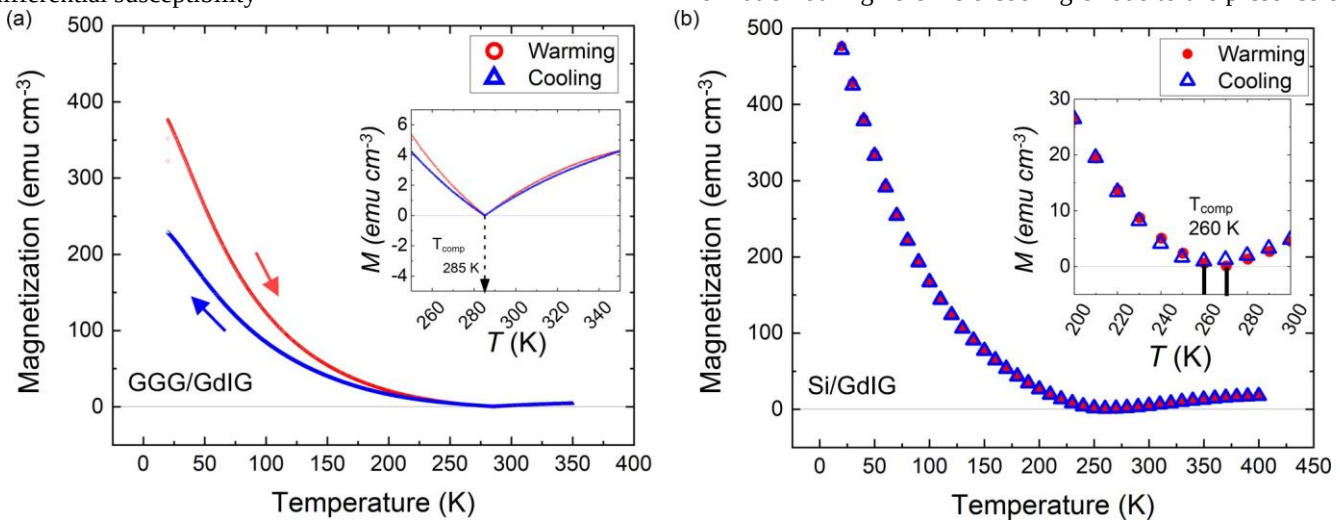

FIG. 3. Temperature-dependent magnetization characteristics of GdIG thin films on (a) lattice-matched GGG (100) recorded at remanence (zero applied field) and (b) Si substrates recorded in a saturating field of 100 mT. Magnetization is recorded in both the warming and cooling sequences. The insets highlight the respective compensation points of the garnet on GGG and Si, and their corresponding magnetization variation.

The temperature dependence of the magnetization of single crystalline GdIG thin films on GGG substrates, shown in Fig. 3(a), reveals the compensation temperature to be 285 K, which is comparable to the reported bulk compensation point of 286 K in GdIG [43]. Interestingly, the magnetization evolution with temperature has a hysteretic behavior between the warming (20–350 K) and cooling (350–20 K) measurement sequences. As seen in Fig. 3(a), at temperatures below 200 K, the warming vs cooling magnetization values diverge and have a difference of 150emu cm^{-3} (1emu cm^{-3} = 1 kA/m) at 20 K. These measurements are performed at zero field to mitigate the paramagnetic background of the GGG. Speficially, a saturation field is applied at 20 K after which the remnant magnetization (at zero field) is recorded continuously as the temperature is swept to 350 K (heating sequence) and immediately swept back to 20 K (cooling sequence). The decreasing magnetization in the heating sequence corresponds to the temperature dependence of the Gd^{3+} sublattice, including the effects of thermal fluctuations at higher temperatures. However, in the cooling sequence, the measured magnetization is only from those moments that undergo a spontaneous magnetization with decreasing temperature. This is smaller than the magnetization from the heating measurements. This is likely due to magnetic domain formation during zero-field cooling or due to the presence of unsaturated and pinned Gd^{3+} moments (from thermalization) that would require a large saturation field, which is not available in the zero-field measurement condition [44]. Clarification of the exact magnetic process that leads to a lower magnetization requires additional characterizations that are unavailable at this time. On the other hand, the polycrystalline GdIG thin films on Si substrates have a compensation temperature of 260 K, as shown in Fig. 3(b). While Gd deficiency undoubtedly plays an important role in determing the compensation temperature, so do the differences in defect density and crystal structure of the GdIG films on GGG and Si. The 30 K difference in compensation temperature, observed here, thus likely reflects the influence of crystal structure or cation site occupancy. On the other hand, unlike the single crystalline films, GdIG on Si did not contain a strong paramagnetic background, which allowed for a measurement in an applied magnetic field. This was sufficient to saturate the sublattice moments and therefore did not show any magnetic hysteresis with temperature.

A comparison of saturation magnetization from molecular field theory (MFT) calculations [43] and superconducting quantum interference device (SQUID) measurements indicates that the latter is smaller than the theoretical estimates. In the thin films of GdIG considered here, the reduced magnetization could be a consequence of Gd and Fe deficient stoichiometry, which lowers the respective sublattice magnetization from the cations. This is evident from the reduced compensation temperature in Si/GdIG samples. However, in the case of single crystal GdIG films with near-ideal compensation, even after scaling the remanent magnetization using the remanence ratio (M_r/M_s) of 0.77, the saturation magnetization falls short of the theoretical prediction as shown in Fig. S6 in the Supplemental Material [40]. Literature reports on GdIG suggest that a range of

magnetic compensation temperatures can exist in thin films despite having favorable bulklike magnetic characteristics [23,31,45]. Therefore, it is likely that nonideal magnetic properties such as reduced magnetization (or compensation temperature) could arise from an inhomogeneous distribution of elemental and structural characteristics. Such inhomogeneities might occur at the film/substrate

FIG. 4. Polarized neutron reflectivity and x-ray reflectivity from GGG/GdIG. (a) X-ray and spin-dependent neutron Fresnel reflectivities from the GGG/GdIG sample, plotted on a log scale as a function of the momentum transfer along the film normal. Neutron data taken at 100 K in 200 and 50 mT. Solid lines are the fitted curves. (b) Difference between the spin-up and spin-down Fresnel neutron reflectivities alongside the best-fit model. Difference curves offset for clarity. (c) Real x-ray (solid blue line), real neutron nuclear (solid black line), imaginary neutron nuclear (dashed green line), and neutron magnetic (red dash-dot line) scattering length density profiles that were used to generate the fits shown. Note that for regions of the neutron SLD curves containing Gd, the maximum and minimum values of the wavelength-dependent SLD values are both plotted, with the region in between shaded. Intermediate wavelengths fall within the shaded region. Error bars represent ±1

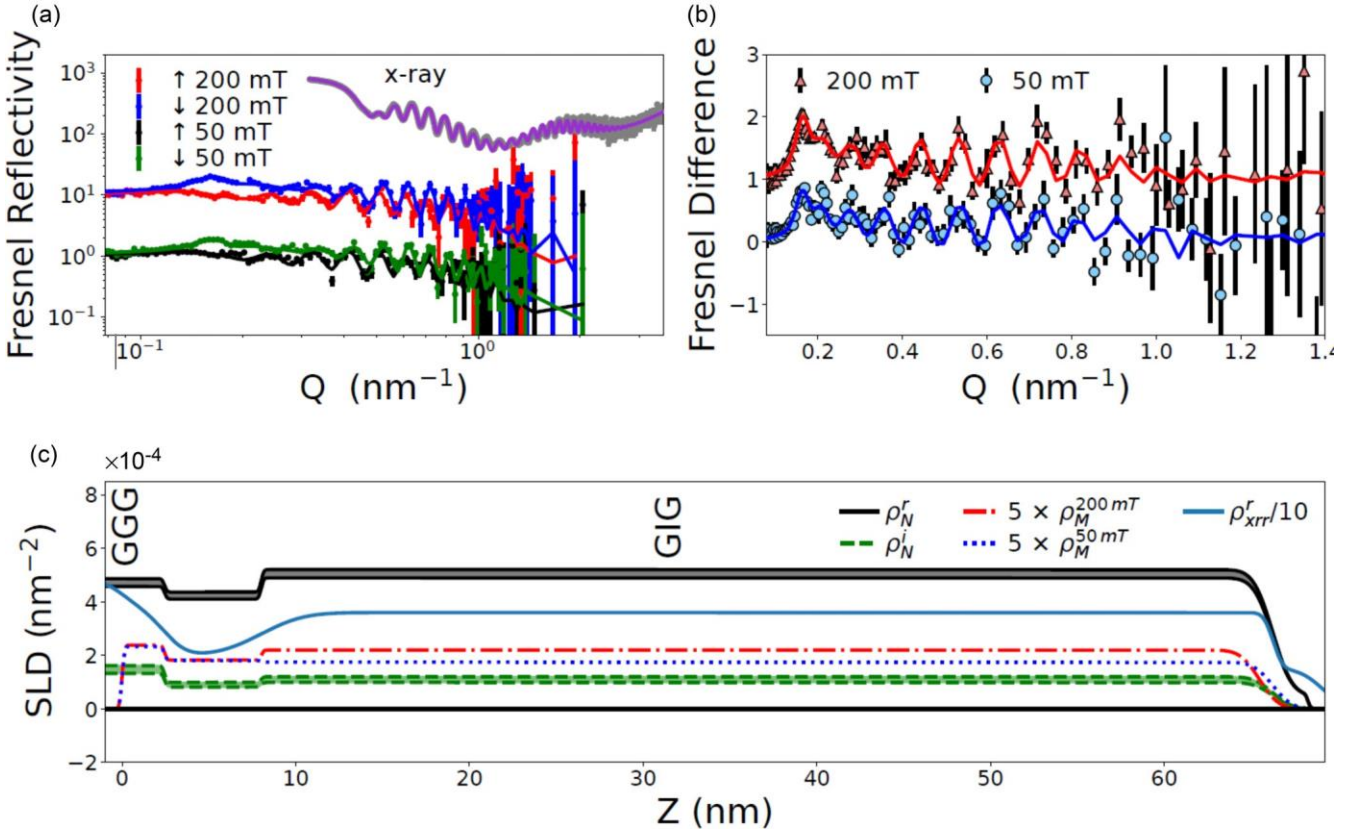

standard deviation.

interface or through the thickness of the film, and cannot be quantified from magnetometry, which only measures the volume-averaged physical properties.

Depth-profile measurements using polarized neutron reflectometry, as shown in Fig. 4, reveal that the majority of the GdIG sample grown on GGG is magnetically and structurally uniform, without magnetically dead layers at either the top or bottom interfaces. Moreover, PNR is very sensitive to the Gd content of the film due to the high absorption cross section for Gd [46]. Therefore, the fitted real and imaginary nuclear SLD profiles shown in Fig. 4(c) may be used to understand the presence of voids and Gd content of the film, respectively, both of which in turn affect the magnetic characteristics. We find that, assuming bulk stoichiometry, the real nuclear SLD is near that of bulk GdIG within the film. Of course, EDS measurements indicate some degree of off-stoichiometry in the form of Gd deficiency. The effect of such off-stoichiometry on the real nuclear SLD is unclear, as removing a relatively large amount of Gd could be offset by a small amount of excess Fe due to the large scattering cross section of Fe. In this case, calculating the expected real nuclear SLD would require both precise density and composition measurements, which is not possible for a thin film on a substrate. On the other hand, the imaginary component of the nuclear SLD profile allows a relatively precise estimation of the Gd number density, which is found to be approximately 77.0% ± 1.2% of the bulk in the GGG/GdIG sample, in relatively good agreement with the EDS measurements.

Of particular note is the GGG/GdIG interface, which exhibits evidence of intermixing and lower-density transitional growth region in the thin film. In this region, we find an approximately 2–3 nm thick magnetized layer of "GGG" which likely contains Fe incorporated from the film and an approximately 5–6 nm thick lower-density transitional region of GdIG which exhibits suppression of the real nuclear SLD, imaginary nuclear SLD, and magnetic SLD relative to the bulk of the film. Note that although fitting the magnitude of the spin splitting above 0.35nm^{-1} was not possible without

magnetization in the interfacial GGG, the sensitivity of the PNR to the precise thickness of this magnetized layer is limited. Without this feature, the oscillations in the theoretical Fresnel difference curve (also called the Fresnel spin difference and defined as $(R^{\uparrow\uparrow}-R^{\downarrow\downarrow})/R_{\text{Substrate}}$) are significantly damped above 0.35nm^{-1}, so that the oscillations in the data are much larger than the theory curve, as shown in Fig. S7 of the Supplemental Material [40] (including Refs. [47–49].

well with bulk magnetization measurements at 100 K, showing a magnetization of approximately 150emu cm^{-3}.

PNR measurements were also performed on the Si/GdIG sample at 100 K in applied fields of 50 and 200 mT as shown in Fig. 5. Analysis of the Si/GdIG sample was complicated by growth on substrates with two polished sides, so that reflections from both the front and back of the sample must be considered. To account for this, the simulated theory curves

FIG. 5. Polarized neutron reflectivity and x-ray reflectivity from Si/GdIG. (a) X-ray and spin-dependent Fresnel reflectivities from the Si/GdIG sample at 100 K in 200 and 50 mT plotted on a log scale as a function of the momentum transfer along the film normal, plotted alongside the fitted curve. Curves from different fields and techniques are offset for clarity. (b) Difference between the spin-up and spin-down Fresnel reflectivities alongside the best-fit model. Difference curves offset for clarity. (c) Real nuclear (solid black line), imaginary nuclear (dashed green line), 200 mT magnetic (red dash-dot line), and 50 mT magnetic (blue dot line) scattering length density profiles used to generate the fits shown. Note that for regions of the SLD curves containing Gd, the maximum and minimum values of the wavelength-dependent SLD values are both plotted, with the region in between shaded. Intermediate wavelengths fall within the shaded region. Error bars represent ±1

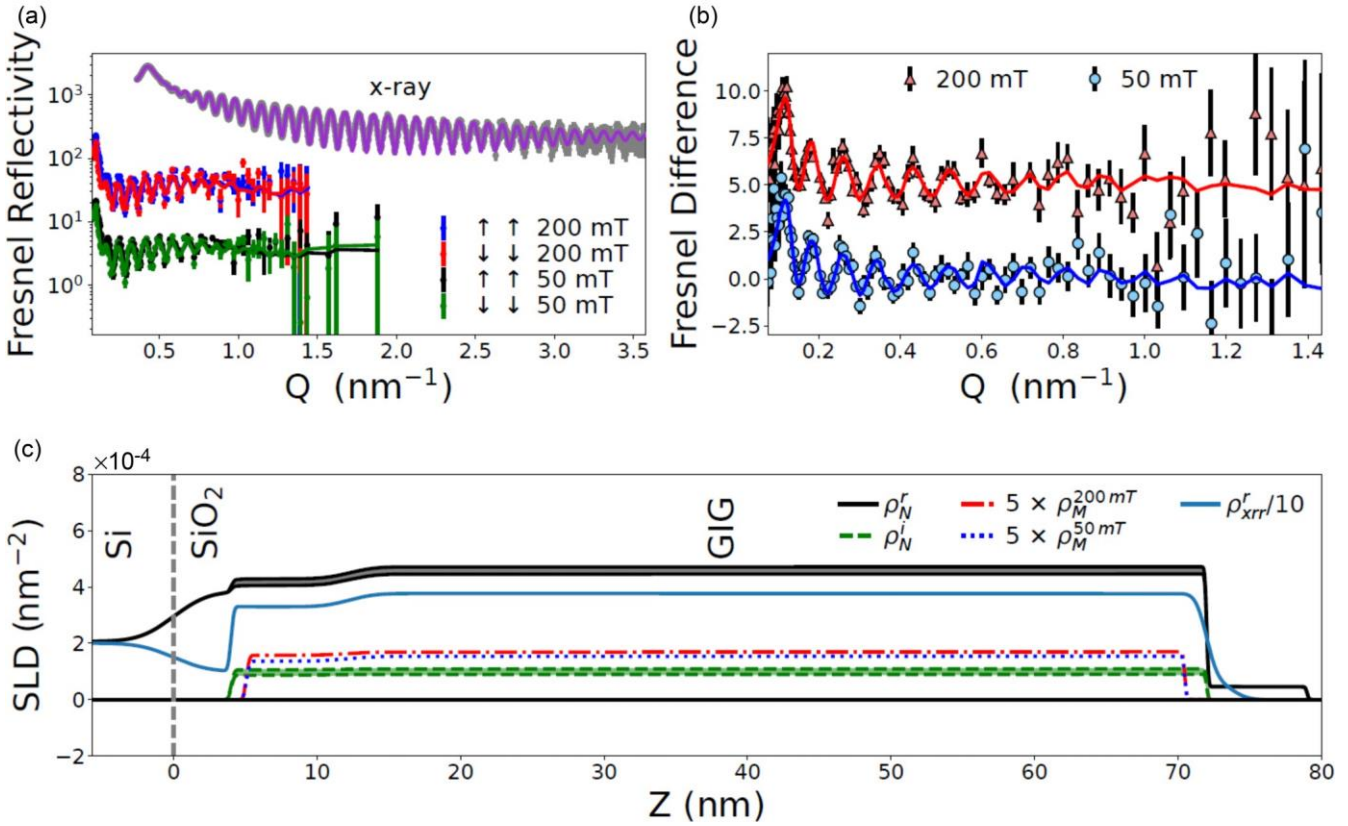

standard deviation.

Models with a magnetic GGG layer, in contrast, yield larger amplitude oscillations in the Fresnel difference at high Q and therefore fit the data much better. Alternative fitting approaches, including magnetically dead layers or gradients in the GdIG composition and magnetization, also failed to fit the data. We conclude that the magnetic GGG region is necessary to properly describe the data. Intermixing at the interface is also consistent with the observation of a second oscillation period in the x-ray reflectivity scans of GGG/GdIG samples in Fig. S8 [40], where the extracted intermixed region thicknesses match the approximate implied thickness of the second layer. The magnetic SLD in the bulk of the film agrees

were calculated using the incoherent sum of two samples, representing the Si/SiO$_2$/air layer structure on the rear of the sample and the Si/SiO$_2$/GdIG/air stack of interest. The native oxide layer was constrained to be identical on both sides of the substrate and fitting such a model naturally converges to an equal weighting of the front and back sides, as expected given their equal cross-sectional areas.

Since the presence of both front and back reflections adds complexity to the model, we added additional constraint by corefining the Si/GdIG dataset with an x-ray reflectivity curve on the same sample. PNR and x-ray models were constrained to have identical thicknesses across models for all datasets. The modeling shows that the majority of the GdIG film is structurally uniform, with a 7nm ± 2 nm region of lower density near the SiO$_2$/GdIG interface as shown in Fig. 5(c).

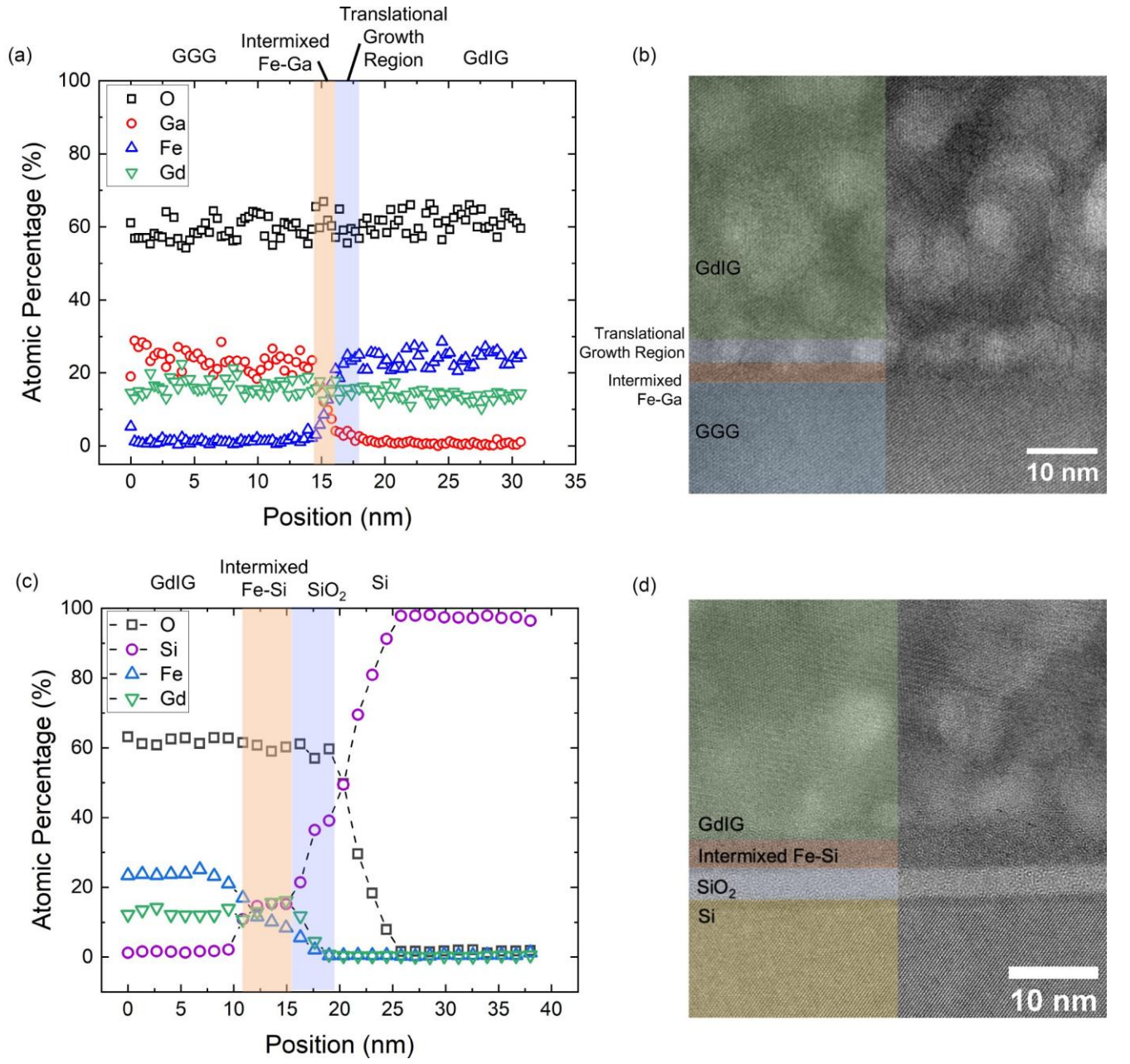

FIG. 6. Interfacial composition and structural characteristics. (a) Composition profile of GGG/GdIG across the interface from STEM-EDS, where the shaded region qualitatively indicates the intermixing of Fe-Ga and the low-density translational growth region at the GGG/GdIG interface. (b) High-resolution TEM image of the GGG/GdIG cross section. (c) Composition profile of Si/SiO_2/GdIG across the substrate-film interface from STEM-EDS, where the shaded regions are SiO_2 and intermixed Fe-Si, respectively. (d) High-resolution TEM image of the Si/SiO_2/GdIG cross section shows the amorphous intermixed region of Fe-Si. The highlighted regions in (a,c) are a guide to the eye, and are

We speculate that this region, with an imaginary SLD similar to the rest of the film but a lower real nuclear SLD, is slightly Fe deficient, in agreement with the STEM EDS shown later. The magnetization is relatively uniform except for a small (1.5nm ± 0.3 nm) magnetically dead layer near the SiO_2/GdIG interface. The GdIG volume fraction was found to be 90.5% ± 0.2%, unlike the GGG/GdIG sample which exhibited a bulklike real nuclear SLD in the GdIG layer. On the other hand, the sample on Si was Gd deficient to a similar degree as the sample on GGG, with approximately 76.2% ± 0.1% of the idealized Gd content. This stoichiometry is within in qualitative agreement with the neutron data.

the uncertainty of the values obtained through EDS. The observed magnetization in this sample was 116emu cm^{-3}, slightly lower than that reported through bulk magnetometry but within the variability expected from sample to sample given the sensitivity to small changes in compensation temperature.

While PNR measurements reveal an intermixed region in GGG/GdIG and a magnetically dead layer at the SiO_2/GdIG

interface, a quantitative assessment of the composition across the interface is required. Here, the interfacial predictions from PNR are corroborated by STEM EDS and HRTEM measurements across the cross section of the GGG/GdIG sample. As shown in Fig. 6(a), several nm of Fe-Ga intermixing is present at the interface, while Fig. 6(b) reveals a larger ∼3–4 nm transitional growth region. Despite the intermixing at the interface, Fig. 6(b) shows continuous lattice fringes extending from GGG to GdIG, indicating that the films are epitaxial. Away from the interface, the stoichiometry of these single crystalline films is uniform but has up to 20% of Gd deficiency, similar to observations from SEM EDS in Si/GdIG samples. On the other hand, in Si/SiO_2/GdIG samples, crosssection STEM EDS [Fig. 6(c)] reveals a 3 nm region of intermixed Fe-Si at the SiO_2/GdIG interface that is Fe deficient as in the previous case. Correlating these measurements with those from SEM EDS shows that the latter fails to account for interfacial stoichiometric variations and could result in overestimation of cation deficiencies even when the bulk of the film maintains near-ideal composition. High-resolution TEM images in Fig. 6(d) suggest that this off-stoichiometric interface likely leads to few monolayers of amorphous GdIG. Furthermore, the amorphous nature of this Fe-deficient interface also explains the formation of a magnetically dead layer as observed from the PNR measurements.

IV. CONCLUSION

In summary, a quantitative characterization of the bulk and interfacial magnetic properties, and composition profiles are provided for sputtered thin films of epitaxial GdIG on GGG and polycrystalline GdIG on Si. While both GGG/GdIG and Si/GdIG have near-room-temperature magnetic compensation points at 286 and 260 K, respectively, the hysteretic-temperature-dependent magnetization in GGG/GdIG is attributed to the unsaturated rare-earth moments in the zero-field measurements. Depth-profile measurements using PNR and cross-section imaging using HRTEM show a strong similarity with high packing fractions in GdIG films grown on GGG and Si substrates. The Gd content of both films is 20% lower than stoichiometric composition, and the magnetizations are similar. The most significant difference between the two films is the presence of voids in Si/GdIG and the nature of the intermixed region at the substrate/GdIG interface. In GGG/GdIG, intermixing of Fe-Ga leads to a magnetization in the surface GGG and a low-density transitional growth region of the GdIG. This constitutes definitive evidence that transition-metal cation intermixing plays a critical role in determining the interfacial magnetic state, rather than being exclusively dominated by rare-earth cation exchange. In the Si/GdIG sample, the Fe-Ga intermixed interface is replaced with a 3 nm Fe-Si intermixed layer that matches the rest of the bulk nuclear SLD in the film, but is magnetically dead. This layer is confirmed qualitatively by high-resolution TEM and STEM EDS measurements. Despite the inhomogeneities at the interface, the structural and elemental characteristics are homogeneous across the bulk of the film, with favorable bulklike magnetic properties and near-room-temperature compensation.

ACKNOWLEDGMENTS

This work was made possible through the Educational Seed Funding Award for 2020 by the IEEE Magnetics Society. Parts of this work were carried out in the Characterization Facility, University of Minnesota, which receives partial support from the NSF through the MRSEC (Award No. DMR-2011401) and the NNCI (Award No. ECCS-2025124) programs. K.S. would like to acknowledge the help from Dr. Dario Bilardello and Mr. Peter Solheid for work performed at the Institute of Rock Magnetism (IRM). The IRM is a U.S. National Multi-user Facility supported through the Instrumentation and Facilities program of the National Science Foundation, Earth Sciences Division (Grant No. NSF-EAR 2153786), and by funding from the University of Minnesota. We would also like to acknowledge the ISIS neutron and muon source for the provision of the neutron beamtime award (Award No. RB2000249) [50]. Work performed at the Center for Nanoscale Materials, a U.S. Department of Energy Office of Science User Facility, was supported by the U.S. DOE, Office of Basic Energy Sciences, under Contract No. DE-AC02-06CH11357. Certain commercial equipment, instruments, software, or materials are identified in this paper in order to specify the experimental procedure adequately. Such identifications are not intended to imply recommendation or endorsement by NIST, nor it is intended to imply that the materials or equipment identified are necessarily the best available for the purpose.

[1] J. Finley and L. Liu, Spintronics with compensated ferrimagnets, Appl. Phys. Lett. **116**, 110501 (2020).

[2] K. Cai, Z. Zhu, J. M. Lee, R. Mishra, L. Ren, S. D. Pollard, P. He, G. Liang, K. L. Teo, and H. Yang, Ultrafast and energy-efficient spin–orbit torque switching in compensated ferrimagnets, Nat. Electron. **3**, 37 (2020).

[3] R. Mishra, J. Yu, X. Qiu, M. Motapothula, T. Venkatesan, and H. Yang, Anomalous current-induced spin torques in ferrimagnets near compensation, Phys. Rev. Lett. **118**, 167201 (2017).

[4] B.-W. Dong, J. Cramer, K. Ganzhorn, H. Y. Yuan, E.-J. Guo, S. T. B. Goennenwein, and M. Kläui, Spin Hall magnetoresistance in the non-collinear ferrimagnet GdIG close to the compensation temperature, J. Phys.: Condens. Matter **30**, 035802 (2017).

[5] G. Winkler, *Magnetic Garnets* (Vieweg, Braunschweig, Germany, 1981).

[6] L. Caretta *et al.*, Fast current-driven domain walls and small skyrmions in a compensated ferrimagnet, Nat. Nanotechnol. **13**, 1154 (2018).

[7] R. Ramos, T. Hioki, Y. Hashimoto, T. Kikkawa, P. Frey, A. J. E. Kreil, V. I. Vasyuchka, A. A. Serga, B. Hillebrands, and E. Saitoh, Room temperature and low-field resonant

enhancement of spin Seebeck effect in partially compensated magnets, Nat. Commun. **10**, 1 (2019).

[8] K. Srinivasan, Y. Chen, L. Cestarollo, D. K. Dare, J. G. Wright, and A. El-Ghazaly, Engineering large perpendicular magnetic anisotropy in amorphous ferrimagnetic gadolinium cobalt alloys, J. Mater. Chem. C **11**, 4820 (2023).

[9] K. Srinivasan, C. Radu, D. Bilardello, P. Solheid, and B. J. H. Stadler, Interfacial and bulk magnetic properties of stoichiometric cerium doped terbium iron garnet polycrystalline thin films, Adv. Funct. Mater. **30**, 2000409 (2020).

[10] A. Quindeau *et al.*, $Tm_3Fe_5O_{12}$/Pt heterostructures with perpendicular magnetic anisotropy for spintronic applications, Adv. Electron. Mater. **3**, 1600376 (2017).

[11] V. H. Ortiz, M. Aldosary, J. Li, Y. Xu, M. I. Lohmann, P. Sellappan, Y. Kodera, J. E. Garay, and J. Shi, Systematic control of strain-induced perpendicular magnetic anisotropy in epitaxial europium and terbium iron garnet thin films, APL Mater. **6**, 121113 (2018).

[12] M. Kubota, A. Tsukazaki, F. Kagawa, K. Shibuya, Y. Tokunaga, M. Kawasaki, and Y. Tokura, Stress-induced perpendicular magnetization in epitaxial iron garnet thin films, Appl. Phys. Express **5**, 103002 (2012).

[13] J. J. Bauer, E. R. Rosenberg, S. Kundu, K. A. Mkhoyan, P. Quarterman, A. J. Grutter, B. J. Kirby, J. A. Borchers, and C. A. Ross, Dysprosium iron garnet thin films with perpendicular magnetic anisotropy on silicon, Adv. Electron. Mater. **6**, 1900820 (2019).

[14] H. Wang, C. Du, P. C. Hammel, and F. Yang, Strain-tunable magnetocrystalline anisotropy in epitaxial $Y_3Fe_5O_{12}$ thin films, Phys. Rev. B **89**, 134404 (2014).

[15] C. L. Jermain, H. Paik, S. V. Aradhya, R. A. Buhrman, D. G. Schlom, and D. C. Ralph, Low-damping sub-10-nm thin films of lutetium iron garnet grown by molecular-beam epitaxy, Appl. Phys. Lett. **109**, 192408 (2016).

[16] A. Mitra *et al.*, Interfacial origin of the magnetisation suppression of thin film yttrium iron garnet, Sci. Rep. **7**, 11774 (2017).

[17] J. F. K. Cooper, C. J. Kinane, S. Langridge, M. Ali, B. J. Hickey, T. Niizeki, K. Uchida, E. Saitoh, H. Ambaye, and A. Glavic, Unexpected structural and magnetic depth dependence of YIG thin films, Phys. Rev. B **96**, 104404 (2017).

[18] Y. Lv *et al.*, Large unidirectional spin Hall and Rashba–Edelstein magnetoresistance in topological insulator/magnetic insulator heterostructures, Appl. Phys. Rev. **9**, 011406 (2022).

[19] E. L. Jakubisova, S. Visnovsky, H. Chang, and M. Wu, Interface effects in nanometer-thick yttrium iron garnet films studied by magneto-optical spectroscopy, Appl. Phys. Lett. **108**, 082403 (2016).

[20] K. Shen, Temperature-switched anomaly in the spin Seebeck effect in $Gd_3Fe_5O_{12}$, Phys. Rev. B **99**, 024417 (2019).

[21] A. Yagmur, R. Iguchi, S. Geprägs, A. Erb, S. Daimon, E. Saitoh, R. Gross, and K. Uchida, Lock-in thermography measurements of the spin Peltier effect in a compensated ferrimagnet and its comparison to the spin Seebeck effect, J. Phys. D: Appl. Phys. **51**, 194002 (2018).

[22] Y. Ohnuma, H. Adachi, E. Saitoh, and S. Maekawa, Spin Seebeck effect in antiferromagnets and compensated ferrimagnets, Phys. Rev. B **87**, 014423 (2013).

[23] S. Geprägs *et al.*, Origin of the spin Seebeck effect in compensated ferrimagnets, Nat. Commun. **7**, 10452 (2016).

[24] L. W. Wang, L. S. Xie, P. X. Xu, and K. Xia, First-principles study of magnon-phonon interactions in gadolinium iron garnet, Phys. Rev. B **101**, 165137 (2020).

[25] J. Xiao, G. E. W. Bauer, K.-c. Uchida, E. Saitoh, and S. Maekawa, Theory of magnon-driven spin Seebeck effect, Phys. Rev. B **81**, 214418 (2010); Erratum: Theory of magnon-driven spin Seebeck effect [Phys. Rev. B 81, 214418 (2010)], **82**, 099904(E) (2010).

[26] H. Maier-Flaig, S. Geprägs, Z. Qiu, E. Saitoh, R. Gross, M. Weiler, H. Huebl, and S. T. B. Goennenwein, Perpendicular magnetic anisotropy in insulating ferrimagnetic gadolinium iron garnet thin films, arXiv:1706.08488.

[27] M. Kuila, Z. Hussain, and V. R. Reddy, MOKE study of magnetic compensation in polycrystalline gadolinium iron garnet thin film, J. Magn. Magn. Mater. **473**, 458 (2019).

[28] H. Maier-Flaig, M. Harder, S. Klingler, Z. Qiu, E. Saitoh, M. Weiler, S. Geprägs, R. Gross, S. T. B. Goennenwein, and H. Huebl, Tunable magnon-photon coupling in a compensating ferrimagnet—from weak to strong coupling, Appl. Phys. Lett. **110**, 132401 (2017).

[29] C. Holzmann, A. Ullrich, O.-T. Ciubotariu, and M. Albrecht, Stress-induced magnetic properties of gadolinium iron garnet nanoscale-thin films: Implications for spintronic devices, ACS Appl. Nano Mater. **5**, 1023 (2022).

[30] K. Ganzhorn *et al.*, Spin Hall magnetoresistance in a canted ferrimagnet, Phys. Rev. B **94**, 094401 (2016).

[31] J. Cramer *et al.*, Magnon mode selective spin transport in compensated ferrimagnets, Nano Lett. **17**, 3334 (2017).

[32] S. Yuasa, K. Hono, G. Hu, and D. C. Worledge, Materials for spin-transfer-torque magnetoresistive random-access memory, MRS Bull. **43**, 352 (2018).

[33] J. J. Bauer, P. Quarterman, A. J. Grutter, B. Khurana, S. Kundu, K. A. Mkhoyan, J. A. Borchers, and C. A. Ross, Magnetic proximity effect in magnetic-insulator/heavy-metal heterostructures across the compensation temperature, Phys. Rev. B **104**, 094403 (2021).

[34] https://www.isis.stfc.ac.uk/Pages/polref.aspx.

[35] J. E. Lynn and P. A. Seeger, Resonance effects in neutron scattering lengths of rare-earth nuclides, At. Data Nucl. Data Tables **44**, 191 (1990).

[36] E. Sawatzky and E. Kay, Cation deficiencies in rf sputtered gadolinium iron garnet films, IBM J. Res. Dev. **13**, 696 (1969).

[37] V. H. Ortiz *et al.*, First- and second-order magnetic anisotropy and damping of europium iron garnet under high strain, Phys. Rev. Mater. **5**, 124414 (2021).

[38] E. R. Rosenberg *et al.*, Magnetism and spin transport in rareearth-rich epitaxial terbium and europium iron garnet films, Phys. Rev. Mater. **2**, 094405 (2018).

[39] G. Yu and J. Garcia Barriocanal, computer code RSLAB, Fast 3-dimensional reciprocal space imaging with laboratory x-ray diffraction: RSLAB, University of Minnesota, 2021.

[40] See Supplemental Material at http://link.aps.org/supplemental/10.1103/PhysRevMaterials.8.044403 for additional information on reciprocal space maps, temperature-dependent magnetometry, polarized neutron reflectometry, Markov-chain Monte Carlo analysis technique, and x-ray reflectivity measurements.

[41] W. P. Wolf and R. M. Bozorth, Susceptibility of gadolinium iron garnet below the Néeel point, Phys. Rev. **124**, 449 (1961).

[42] J. P. Hanton, Intrinsic coercive force of rare earth iron garnets near the compensation temperature, IEEE Trans. Magn. **3**, 505 (1967).

[43] P. Hansen, K. Witter, and W. Tolksdorf, Magnetic and magnetooptical properties of bismuth-substituted gadolinium iron garnet films, Phys. Rev. B **27**, 4375 (1983).

[44] M. Lahoubi, M. Guillot, A. Marchand, F. Tcheou, and E. Roudault, Double umbrella structure in terbium iron garnet, IEEE Trans. Magn. **20**, 1518 (1984).

[45] A. Chanda, C. Holzmann, N. Schulz, J. Seyd, M. Albrecht, M.H. Phan, and H. Srikanth, Scaling of the thermally induced sign inversion of longitudinal spin Seebeck effect in a compensated ferrimagnet: Role of magnetic anisotropy, Adv. Funct. Mater. **32**, 2109170 (2022).

[46] V. F. Sears, Neutron scattering lengths and cross sections, Neutron News **3**, 26 (1992).

[47] J. A. Vrugt, C. J. F. ter Braak, C. G. H. Diks, B. A. Robinson, J. M. Hyman, and D. Higdon, Accelerating Markov chain Monte Carlo simulation by differential evolution with self-adaptive randomized subspace sampling, Int. J. Nonlinear Sci. Numer. Simul. **10**, 273 (2009).

[48] P. A. Kienzle, J. Krycka, N. Patel, and I. Sahin, (2011). BUMPS (Version 0.9.1), computer software, University of Maryland, College Park, MD. Retrieved Dec 15, 2023.

[49] P. A. Kienzle, J. Krycka, N. Patel, and I. Sahin, REFL1D (Version 0.8.16), computer software, University of Maryland, College Park, MD. Retrieved Jan 05, 2024.

[50] STFC Home, https://data.isis.stfc.ac.uk/doi/STUDY/ 113614695/.